

Communication

Effect of High-Density Nanoparticles on Recrystallization and Texture Evolution in Ferritic Alloys

Eda Aydogan^{1,2,*}, Connor J. Rietema³ , Ursula Carvajal-Nunez¹, Sven C. Vogel¹ , Meimei Li⁴ and Stuart A. Maloy¹

¹ Los Alamos National Laboratory, Los Alamos, NM 87545, USA; carvajal.ursula@gmail.com (U.C.-N.); sven@lanl.gov (S.C.V.); maloy@lanl.gov (S.A.M.)

² Integrated Manufacturing Center, Sabanci University, Istanbul 34906, Turkey

³ Colorado School of Mines, Golden, CO 80401, USA; crietema@mines.edu

⁴ Argonne National Laboratory, Lemont, IL 60439, USA; mli@anl.gov

* Correspondence: eaydogan@sabanciuniv.edu

Received: 17 March 2019; Accepted: 21 March 2019; Published: 24 March 2019



Abstract: Ferritic alloys are important for nuclear reactor applications due to their microstructural stability, corrosion resistance, and favorable mechanical properties. Nanostructured ferritic alloys having a high density of Y-Ti-O rich nano-oxides (NOs < 5 nm) are found to be extremely stable at high temperatures up to ~1100 °C. This study serves to understand the effect of a high density of nano-particles on texture evolution and recrystallization mechanisms in ferritic alloys of 14YWT (14Cr-3W-0.4Ti-0.21Y-Fe wt %) having a high density of nano-particles and dispersion-free FeCrAl (13Cr-5.2Al-0.05Y-2Mo-0.2Si-1Nb wt %). In order to investigate the recrystallization mechanisms in these alloys, neutron diffraction, electron backscattered diffraction, and in situ and ex situ transmission electron microscopy have been utilized. It has been observed that even though the deformation textures of both the 14YWT and FeCrAl alloys evolved similarly, resulting in either the formation (in FeCrAl alloy) or increase (in 14YWT) in γ -fiber texture, the texture evolution during recrystallization is different. While FeCrAl alloy keeps its γ -fiber texture after recrystallization, 14YWT samples develop a ε -fiber as a result of annealing at 1100 °C, which can be attributed to the existence of NOs. In situ transmission electron microscopy annealing experiments on 14YWT show the combination and growth of the lamellar grains rather than nucleation; however, the recrystallization and growth kinetics are slower due to NOs compared to FeCrAl.

Keywords: nano-structured ferritic alloys (NFAs); FeCrAl alloys; nano-oxides (NOs); neutron diffraction; texture; recrystallization

1. Introduction

Ferritic steels are good candidates for nuclear reactor applications, due to their microstructural stability, corrosion resistance, and favorable mechanical properties [1,2]. For instance, FeCrAl alloys are considered as candidates for the fuel cladding of light water reactors, due to their excellent corrosion resistance and mechanical properties. Moreover, nanostructured ferritic alloys (NFAs) are considered to be as one of the best candidates for structural components in next-generation reactors which are designed to operate at high temperatures and neutron damage levels, due to the existence of nano-oxides (NOs) [3–5]. In order to optimize the processing parameters to produce fuel cladding tubes, it is critical to understand the microstructure evolution during thermo-mechanical processing, e.g., hot rolling and annealing. While low-density large particles have no considerable effects on the recrystallization of the alloys, the high density of the nanoparticles pin the grain boundaries, and

they might affect the evolution of recrystallization. Especially in NFAs, it has been shown that NOs have a paramount effect on the recrystallization and texture evolution. It has been reported that recrystallization and grain growth occur in the rolling direction in the materials with NOs, resulting in anisotropic microstructures [6–8]. This has been ascribed to be resulted from anisotropic pinning effect of NOs aligned in the direction of deformation. Moreover, due to the existence of large amounts of stored energy and Zener pinning, which are caused by the NO pinning of the grain boundaries, large instabilities occur in the microstructure, resulting in abnormal grain growth in these alloys [8–10]. Additionally, the NO-dislocation interaction mechanism, which is proposed to result in dissolution and reprecipitation of NOs, is reported to result in abnormal grain growth in these materials [11].

Texture development after phase transformation, deformation, and recrystallization in bcc materials, especially in steels, has been studied extensively [8,12–14]. It has been found that transformation textures occur on {001}<110> and {332}<113>. However, {332}<113> is transformed into {111}<110> with deformation [15]. Therefore, α - and γ -fiber textures, especially {001}<110>, {111}<110>, {111}<112> and {112}<110> are typical cold rolling textures in iron and low-carbon steels [16]. On the other hand, it has been shown that room temperature-60% compressed 14YWT alloys show {112}<110> and {112}<111> texture components during annealing [8], in contrast to the conventional recrystallization textures in the body centered cubic alloys described in detail by Holscher et al. [17]. However, the mechanism by which the NOs in this alloy change the texture evolution remains unclear, hampering the optimization of processing routes or predictive capabilities of the microstructure evolution for these materials.

In the present paper, we have investigated the effects of a high density of nano-particles on the texture and recrystallization in 14YWT alloys (with a nominal composition of 14Cr-3W-0.4Ti-0.21Y-Fe wt %) and compared it with dispersion-free FeCrAl alloys (with a nominal composition of 13Cr-5.2Al-0.05Y-2Mo-0.2Si-1Nb wt %). Neutron diffraction, electron back scattered diffraction, in situ and ex situ transmission electron microscopy have been utilized to understand the recrystallization mechanisms in these two types of alloys.

2. Materials and Methods

FeCrAl alloys (with a nominal composition of 13Cr-5.2Al-0.05Y-2Mo-0.2Si-1Nb wt %) were produced by casting followed by hot extrusion. The cast ingots were provided from Sophisticated Alloys, Inc. (SAI), Butler, PA. The ingots were homogenized at 1200 °C and hot-extruded at Oak Ridge National Laboratory by using a 1250 ton extrusion press. The extrusion of FeCrAl rods was performed at 800 °C with a reduction ratio of 6.6. 14YWT alloys (with a nominal composition of 14Cr-3W-0.4Ti-0.21Y-Fe wt %) were produced by mechanical alloying, followed by hot extrusion and hot cross rolling, as described in Refs [14,18]. After the initial ball milling, the powders were sealed and degassed at 400 °C. The canned powders were then hot extruded at 850 °C followed by an intermediate annealing at 1000 °C for 1 h. Final cross rolling was performed at 1000 °C to ~50% of thickness reduction, resulting in ~10 mm thick plates. Six millimeter diameter cylinders were cut, with the cylinder axis parallel to the rod axis in the case of FeCrAl alloys, and with the cylinder axis in the plate through-thickness direction in the case of the 14YWT alloys, using electrical discharge machining (EDM). Those cylinders were compressed to 60% engineering strain at room temperature. Annealing experiments were conducted at 1000 °C and 1100 °C for 0.5, 1, 2, 3, and 4 h, in the case of the FeCrAl and 14YWT alloys, respectively, under a vacuum of $\sim 2 \times 10^{-4}$ mbar.

Bulk texture measurements were performed at room temperature by neutron diffraction on a HIPPO (the High Pressure Preferred Orientation) instrument at a pulsed neutron spallation source at LANSCE [19]. Samples were glued onto standard HIPPO holders which were located ~9 m from the neutron moderator. Diffracted neutrons were collected by 1240 ³He tubes arranged on panels distributed over five conical rings, and the samples were rotated around the vertical axis at 0, 67.5, and 90°. The diffraction data was analyzed by Rietveld analysis using the E-WIMV texture algorithm with a 10° resolution of the orientation distribution function (ODF). Moreover, the microstructure and

recrystallization fractions were determined by electron backscattered diffraction (EBSD), using an FEI Inspect field emission gun (FEG) scanning electron microscope (SEM), equipped with a TSL EBSD detector. Ex situ transmission electron microscopy (TEM) and energy dispersive X-ray scattering (EDX) were conducted to determine the distribution and types of the second-phase particles. Line scans across the grain boundaries were performed along the lines having different lengths, depending on the size of the particles, with ~1.5 s dwell times using the FEI Tecnai F30 microscope at 300 kV equipped with an EDAX EDX detector. In order to observe the mechanism of microstructure evolution at the temperature of ex situ annealing—1100 °C, in situ annealing experiments were performed using an intermediate voltage electron microscope (IVEM) at the same temperature, at Argonne National Laboratory. For this experiment, a Gatan high-temperature holder having a Tantalum furnace was utilized, with a heating rate of ~50 °C/min. Also, a Gatan OneView camera with a resolution of 4000 by 4000 was used to capture video during annealing. It should be noted that for the samples for EBSD, in situ and ex situ TEM investigations were prepared by jet electropolishing (using a Tenupol-5 equipment), using a solution of perchloric acid (5%) and methanol at –40 °C with an applied voltage of 20 V.

3. Results and Discussion

Figure 1a,b show the orientation maps of FeCrAl and 14YWT alloys, respectively, in the as-received condition. While orientation of the grains is random in the FeCrAl alloy, they are mostly oriented along the normal direction, parallel to the $\langle 100 \rangle$ with smaller amount oriented in the $\langle 111 \rangle$ directions in 14YWT alloy. The arrows in Figure 1b indicate rolling and extrusion directions. Moreover, while the FeCrAl alloy has large grains of 50–400 μm , the 14YWT alloy has a much finer grain size of ~0.5 μm with a multimodal grain size distribution [14]. Figure 1c,d show the brightfield TEM (BFTEM) images of the microstructures of these alloys. The FeCrAl alloy has a low fraction of second-phase particles having sizes ranging between ~100 nm and ~3 μm . On the other hand, 14YWT alloys have a high density ($\sim 6 \times 10^{23} \text{ m}^{-3}$) of NO (Y-Ti-O) particles [18,20–22]. The red arrows in these figures indicate the second-phase particles. It should be noted that there are other Ti-Si-O-N, Al-O, and Y-O rich particles in 14YWT, as described in [18]. However, their volume fraction is extremely low compared to the volume fraction of NOs. As in the first study on this composition of FeCrAl alloy, the composition of the second-phase particles has been investigated as shown in Figure 1e. Fifteen different particles were characterized by EDX, and three different compositions of particles were found. Note that the elements having high counts (such as Cr and Fe) are plotted separately (top plot) to the ones having low counts. A particle having a size ~3 μm is found to be enriched in all the elements, in the composition of these alloys, besides having Na-Mg-Cl. The smaller particle, having a size of ~250 nm is enriched mostly in Cu. There is a small amount of Mo and Nb enrichment, together with Fe and Cr depletion. Another small particle having a size ~150 nm is found to be rich in Fe, Cr, Mo, Nb, O, N, and C. Na, Mg, Cl, and Cu are presumed to be impurities that were picked up during the processing of these alloys.

Figure 2 shows the evolution of bulk texture as determined by neutron diffraction in FeCrAl and 14YWT alloys after compressing to 60% and annealing at 1000 °C and 1100 °C, respectively, for 4 h. No recrystallization in 14YWT alloys was observed at 1000 °C, even after several hours of annealing (up to 30 h) [5,8], therefore recrystallization studies have been conducted at 1100 °C. In the as-received condition, the texture of FeCrAl alloy is almost random (Figure 2(a-1)) while the 14YWT alloy has a strong texture along $\langle 110 \rangle \parallel \text{RD}$ and $\langle 100 \rangle \parallel \text{ND}$, and a weak texture of $\langle 111 \rangle \parallel \text{ND}$ (Figure 2(b-1)). After 60% compression along ND, the FeCrAl alloy shows strong texture of $\langle 111 \rangle \parallel \text{ND}$ (Figure 2(a-2)). Similarly, while the 14YWT alloy preserves its as-received texture types, the strength of $\langle 110 \rangle \parallel \text{RD}$ texture decreases, and the strength of $\langle 111 \rangle \parallel \text{ND}$ increases with overall increased texture strength after 60% compression (Figure 2(b-2)). In other words, the texture evolution in both FeCrAl and 14YWT under compression is similar (increase in the strength of $\langle 111 \rangle \parallel \text{ND}$ texture component), meaning that the existence of NOs has no significant effect on the texture evolution under deformation. This indeed confirms our texture simulations using the viscoplastic self-consistent (VPSC) model [8], predicting the plastic deformation of polycrystals and the texture development during rolling, as

defined by Lebensohn et al. [23]. In FeCrAl alloy, within ~2 h of annealing at 1000 °C, the strength of texture decreases and remains almost constant with further annealing, while still showing γ -fiber along $\langle 111 \rangle \parallel \text{ND}$ (Figure 2(b-3)–(b-7)). In the case of the 14YWT alloy, the texture strength decreases within an hour of annealing at 1100 °C (still remaining high); however, it fluctuates overtime (Figure 2(b-3)–(b-7)). Moreover, while the $\langle 100 \rangle \parallel \text{ND}$ texture remains still strong, the strength of the γ -fiber along $\langle 111 \rangle \parallel \text{ND}$ increases, indicating that some of the recrystallized grains are oriented along the normal direction. The changes in the texture types and the planes/directions are explained on the ODF sections in the following paragraph.

Texture types can be determined by ODF analysis, as shown in Figure 3. Similar to the pole figures, while the texture is random in the case of the as-received condition of the FeCrAl alloy (Figure 3(a-1)), its strength increases, and the γ -fiber dominates after 60% compression (Figure 3(a-2)). Annealing at 1000 °C decreases the strength of the texture; however, the γ -fiber still dominates the microstructures of the FeCrAl alloy (Figure 3(a-3)–(3-7)). In the case of the 14YWT alloy, there is already presence of a strong α -fiber, together with a weaker γ -fiber in as received condition (Figure 3(b-1)). On the other hand, the γ -fiber becomes stronger after 60% compression (Figure 3(b-2)). Different from the texture evolution in the case of the FeCrAl alloys, α -fiber and ϵ -fiber become more prominent as a result of annealing at 1100 °C (Figure 3(b-3)–(b-7)). In other words, even though the deformation textures of both the 14YWT and FeCrAl alloys are similar (γ -fiber), the texture evolution during the recrystallization is different. While the FeCrAl alloy keeps their γ -fiber texture after recrystallization, the 14YWT sample develops an ϵ -fiber having a $\{112\} \langle 111 \rangle$ texture component, as a result of 1100 °C annealing, which can be attributed to the existence of NOs.

The texture type for the FeCrAl alloy remains same with increasing annealing time at 1000 °C; however, texture strength decreases considerably after 0.5 h of annealing, and it remains almost constant after 2 h of annealing at this temperature. In other words, in FeCrAl, almost 100% recrystallization occurs within 2 h of annealing at 1000 °C (see Figure 2a). Moreover, Supplementary Materials Figure S1 shows the grain size is much smaller compared to the as-received grain size, meaning that the grains are mostly recrystallized. In addition, the kernel average misorientation (KAM) map, which quantifies the accumulated misorientation within the neighborhood of a selected point with respect to a defined set of nearest neighbor points [24], shows that there is almost no strain in the microstructure. This also indicates an almost complete recrystallization of the material after 2 h of annealing at 1000 °C, similar to the findings from the pole figures and the ODF sections in Figures 2a and 3a. Even though a decrease in the texture index in FeCrAl alloys indicate some degree of random orientation of recrystallized grains, existence of the $\langle 111 \rangle \parallel \text{ND}$ texture after 100% recrystallization indicates that there is an oriented growth recrystallization texture rather than oriented nucleation in this alloy as there is no preferred orientation in the newly nucleated grains (see Supplementary Figure S1) [25,26]. On the other hand, the 14YWT alloy shows a slight decrease in their texture strength within 0.5 h of annealing at 1100 °C while texture strength remains high and fluctuates in time after annealing at 1100 °C for 4 h. This fluctuation of texture strength can be attributed to either the variations in the texture in different 14YWT samples or grain boundary pinning of the NOs, as discussed in Ref [8]. It should be noted that the relative strength of the $\langle 111 \rangle \parallel \text{ND}$ component increases after annealing, indicating an increase in the recrystallization amount [17]. However, different than the other bcc recrystallization textures, the $\{112\} \langle 111 \rangle$ component becomes more prominent, which is attributed to the effect of the NOs on texture evolution. On the other hand, the existence of a strong α -fiber even after 4 h of annealing proves the existence of a high fraction of unrecrystallized grains in the material [27]. Similar to the pole figures and the ODF sections obtained by neutron diffraction, the EBSD maps (see Supplementary Figure S2) clearly indicate that even after 4 h of annealing at 1100 °C, there is a large portion of small grains in the 14YWT alloys. The KAM maps prove that these small grains are highly strained regions without any recrystallization while there are strain-free regions of recrystallized and abnormally grown grains. Moreover, the orientation maps indicate that

unrecrystallized grains keep their orientations of $\langle 100 \rangle \parallel \text{ND}$ after annealing. On the other hand, recrystallized and abnormally grown grains show relatively random orientations.

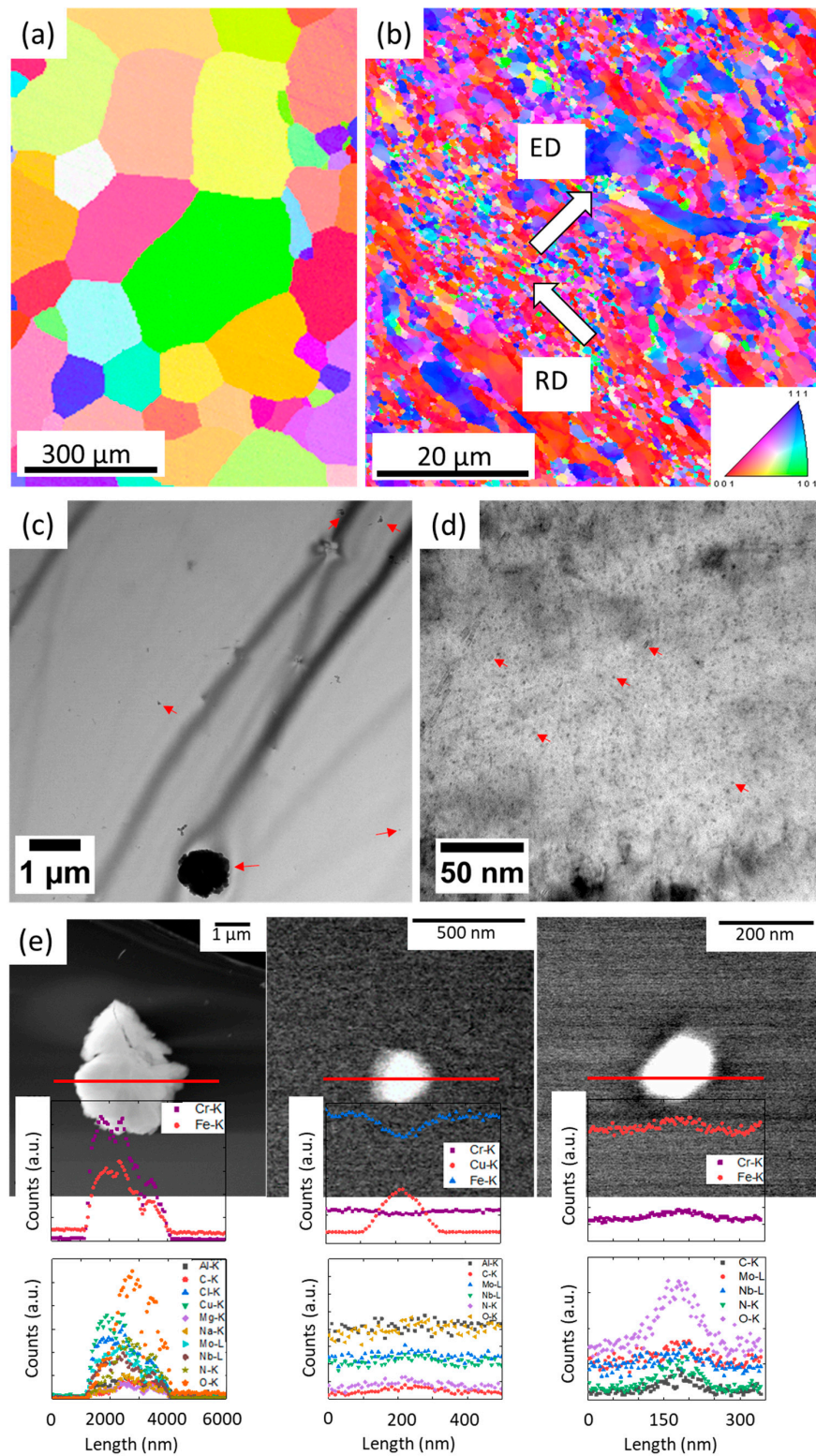


Figure 1. Orientation mapping of (a) FeCrAl and (b) 14YWT alloys; BFTEM micrographs of (c) FeCrAl and (d) 14YWT alloys, (e) EDX line scans along three different particles in FeCrAl alloy. White arrows in (b) indicate the extrusion and rolling directions of the 14YWT alloys. Red arrows in (c) and (d) indicate the second phase particles and NOs, respectively.

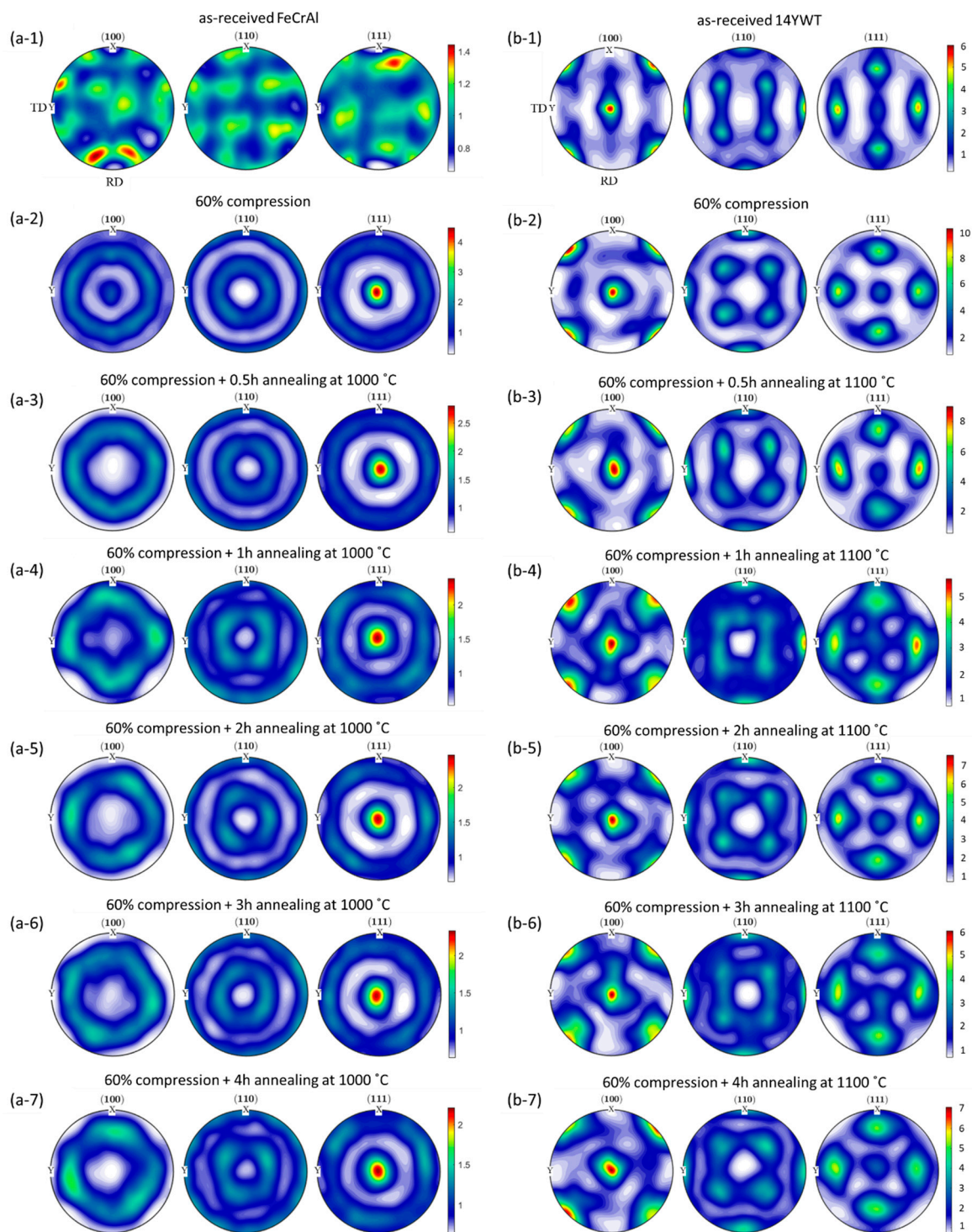


Figure 2. Pole figures showing the evolution of the texture after deforming to 60% and annealing ((a-1) to (a-7)) at 1000 °C for up to 4 h in the FeCrAl alloy, and ((b-1) to (b-7)) at 1100 °C up to 4 h in the 14YW7 alloy.

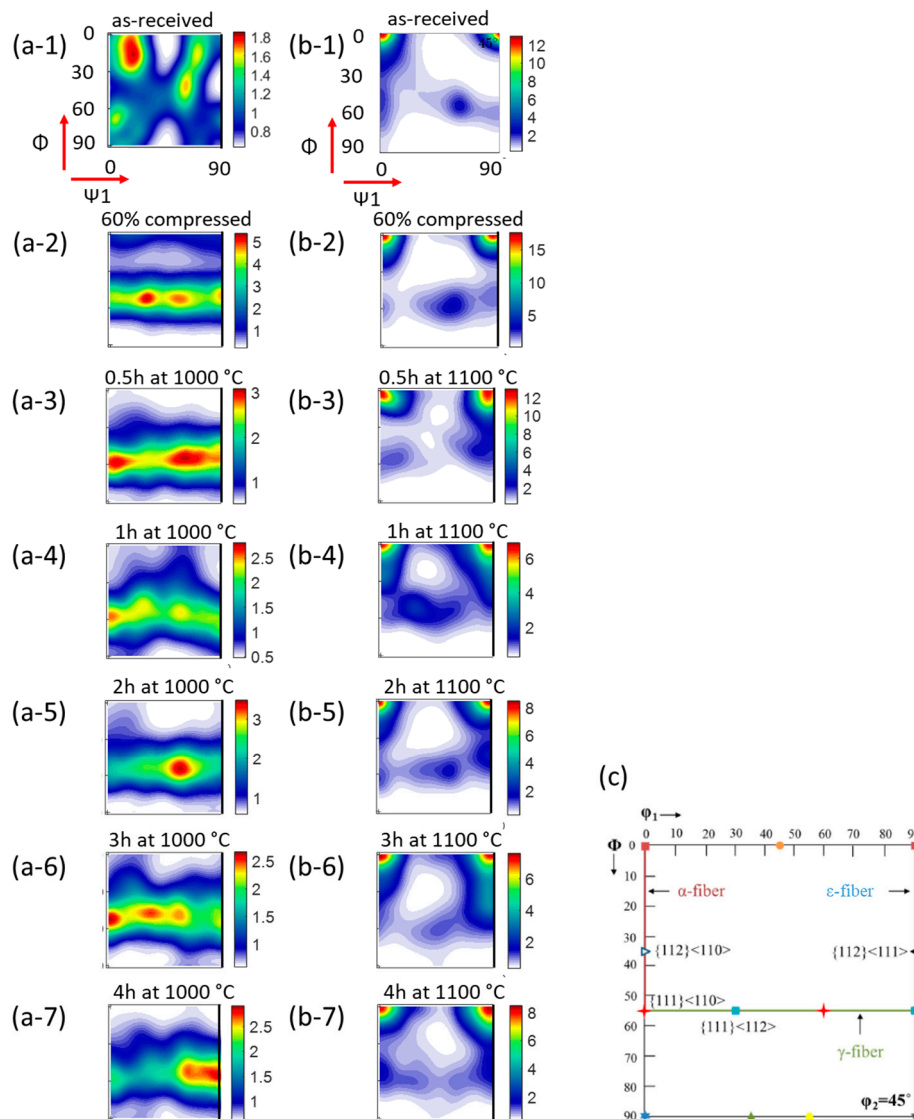


Figure 3. ODF sections of $\Psi_2 = 45^\circ$ for (a) 60% compressed and 1000 °C annealed FeCrAl samples, (b) 60% compressed and 1100 °C annealed 14YWT samples, (c) Schematic illustration of the important texture components in bcc materials [24].

The kinetics of isothermal recrystallization can be described by the Johnson–Mehl–Avrami–Kolmogorov (JMAK) equation [28–30]:

$$X_{rex} = 1 - \exp(-Bt^n) \quad (1)$$

where X_{rex} is the fraction of recrystallization, B is a temperature-dependent constant, t is the isothermal annealing time, and n is the Avrami exponent, which is a function of both the nucleation and growth rates. Equation (1) can be written as Equation (2):

$$\ln \left[\ln \left(\frac{1}{1 - X_{rex}} \right) \right] = n \ln t + \ln B \quad (2)$$

Figure 4a,c show the recrystallization amount vs time plots for the FeCrAl and 14YWT alloys, respectively. In the FeCrAl alloy, ~60% of recrystallization occurs within half an hour of annealing, and recrystallization is completed within 3 h of annealing at 1000 °C. On the other hand, the fraction of recrystallization in 14YWT is ~5% within half an hour of annealing and increases to 10–15% after 4 h of

annealing at 1100 °C. Figure 4b,d show the plots of Equation (2), where the slopes of the straight lines result in the Avrami exponent, n . The Avrami exponents for FeCrAl and 14YWT alloys can be found as 1 and 0.45, respectively. Theoretically, $n = 2$ corresponds to 2D growth while $n = 3$ corresponds to 3D growth, assuming site-saturated nucleation during recrystallization [31]. On the other hand, low n values have been reported for ferritic alloys in the literature. For instance, Malekjani et al. [32] reported the Avrami exponents for ferritic and austenitic alloys between 0.75 and 1.1. Moreover, Xie et al. reported Avrami exponents of 0.5–0.6 for low-carbon steels having relatively high densities of sulfide particles [33]. Garcia-Mateo et al. [34] found this coefficient to be 0.4 in a V-containing steel, due to the existence of V(C,N) particles. Similarly, Shen et al. [6] reported Avrami exponents between 0.4 and 0.9 for 12Cr ODS alloys. These lower values, in the case of ferritic alloys having a high density of second-phase particles, have been attributed to the strong grain boundary pinning by the precipitates, which delays the recrystallization considerably in these materials. Even though the Avrami exponent of FeCrAl alloy is low, the second phase particles in FeCrAl alloy do not have a profound effect on the recrystallization behavior of the alloys. On the other hand, high-density NOs retard recrystallization considerably.

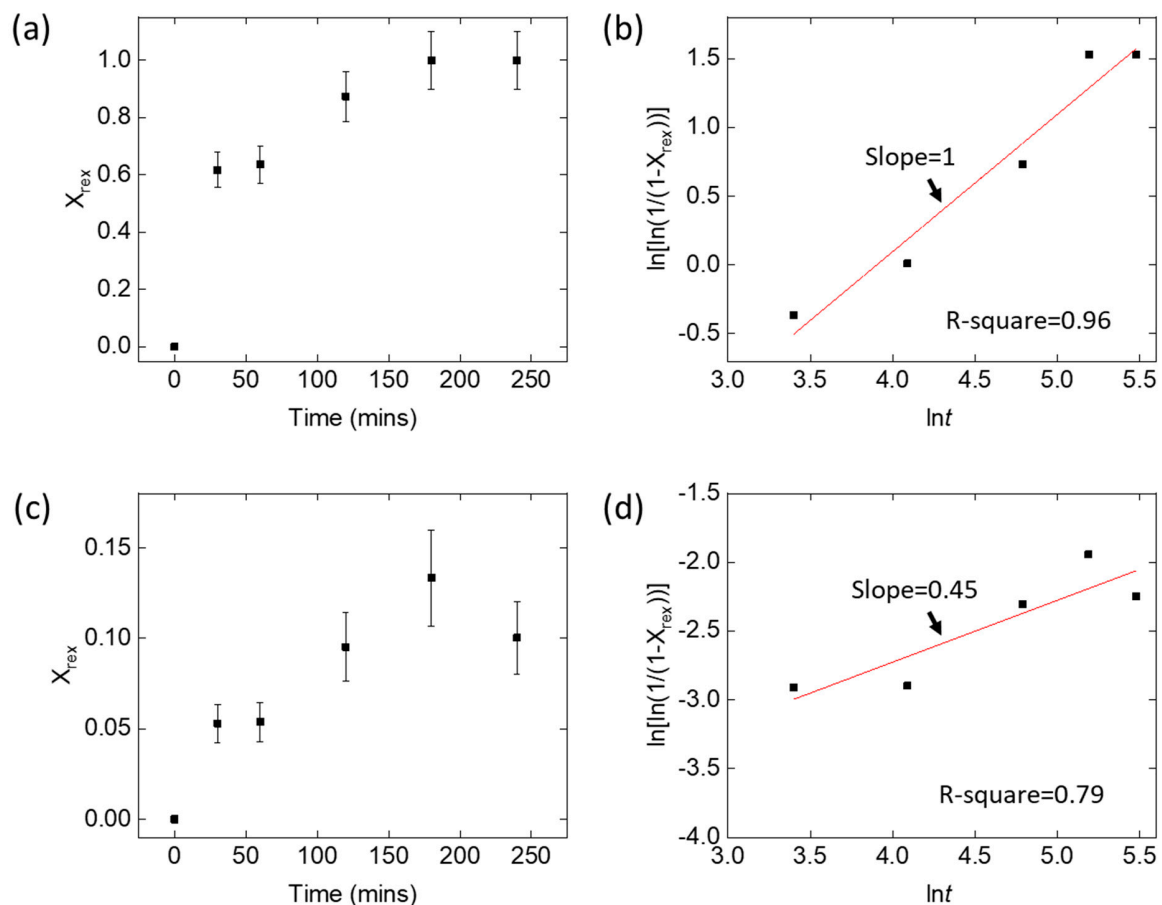


Figure 4. (a) Recrystallization fraction as a function of time, (b) plot of $\ln[\ln(1/(1 - X_{rex}))]$ as a function of $\ln t$ in the FeCrAl alloy annealed at 1000 °C; (c) recrystallization fraction as a function of time, (d) plot of $\ln[\ln(1/(1 - X_{rex}))]$ as a function of $\ln t$ in the 14YWT alloy annealed at 1100 °C.

14YWT alloys are extremely stable at high temperatures. In 60% compressed samples, recrystallization and growth start at 1100 °C; however, even at this temperature, the kinetics are sluggish. While ~5% is recrystallized after 30 min of annealing, only ~10% is recrystallized after 4 h of annealing at this temperature. Figure 5 shows the microstructure evolution at 1100 °C under TEM. After 6.5 min of annealing at 1100 °C, there are subtle changes in the microstructure. Rather than the

nucleation of new grains, two lamellar grains combine and form a thicker grain, while some part of the initial grain remains unchanged, as indicated by the white arrows in Figure 5. Supplementary Video I also shows the in situ evolution of grain structure at 1100 °C. This indicates that at the beginning, secondary recrystallization, which can be nominated as abnormal grain growth, is the dominant mechanism in this alloy, rather than primary recrystallization which results in the formation of strain-free new equiaxed grains. However, after half an hour of annealing at 1100 °C, a few strain-free equiaxed grains could be seen, agreeing with our previous findings and the literature reporting the simultaneous occurrence of recrystallization and abnormal grain growth at above 850 °C [8,9]. In 14YWT alloys, due to the existence of different volume-fraction nanoparticles inside different grains and bimodal grain size distributions, the stored energy throughout the microstructure is not homogenous [8]. These were reported to be the main reasons for abnormal grain growth in materials having nanoparticle dispersions. Therefore, the recrystallization behavior is closely related to the nano-particle and dislocation contents, as well as the sizes of the subsequent grains. The initial dominance of the abnormal grain growth in this study can be attributed to the large inhomogeneity in the microstructure as a result of the extensive deformation.

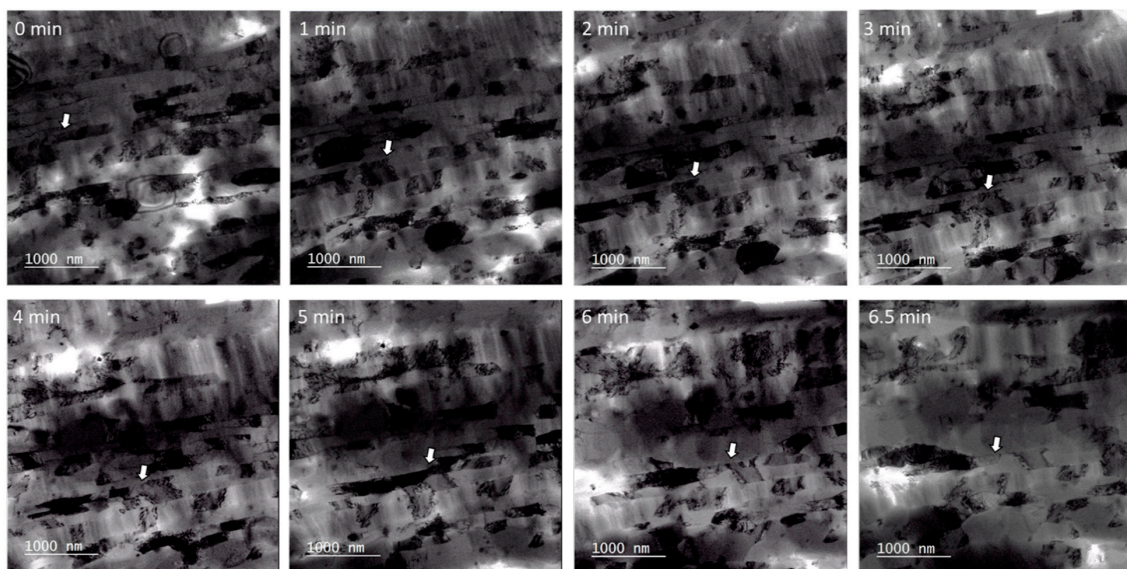


Figure 5. Snapshots of the microstructure evolution in 60% compressed 14YWT alloys at 1100 °C. The white arrows indicate the region evolving in time.

In conclusion, existence of a high-density of nanoparticles affect the texture and recrystallization mechanisms considerably. Even though the texture evolution after 60% compression is similar in FeCrAl and 14YWT alloys, the existence of the nanoparticles in 14YWT results in an ϵ -fiber having a $\{112\}\langle 111 \rangle$ texture component, which is different than FeCrAl alloy. Overall, sluggish recrystallization kinetics have been observed in both the FeCrAl and 14YWT alloys. However, the Avrami coefficient for the FeCrAl alloy has been found to be ~ 2 times larger than the one for the 14YWT alloy. In other words, the recrystallization kinetics are much slower in the 14YWT alloy due to the existence of a high density of NOs. KAM maps confirm the complete recrystallization of the FeCrAl alloys within 2–3 h of annealing at 1000 °C, while 10–15% recrystallization occurs in the case of the 14YWT alloys after annealing at 1100 °C for 4 h. Changes in the texture strength on the pole figures and ODF sections also indicate this behavior. Additionally, in situ TEM microscopy annealing experiments on 60% compressed 14YWT alloy support the slow recrystallization mechanisms in these alloys, showing that the abnormal grain growth occurs dominantly, together with some primary recrystallization due to a large inhomogeneity in the microstructure as a result of extensive deformation.

Supplementary Materials: The following are available online at <http://www.mdpi.com/2073-4352/9/3/172/s1>, Figure S1: (a) Orientation (b) gray scale and (c) kernel average misorientation maps of FeCrAl alloy annealed at 1000 °C for 2 h.; Figure S2: The gray scale, orientation and KAM maps of 14YWT alloys after (a) 0.5 h (b) 1 h (c) 2 h (d) 3 h and (e) 4 h of annealing at 1100 °C. Scales of all the micrographs are the same.

Author Contributions: E.A. designed and performed the experiments, and wrote the manuscript. C.J.R., U.C.-N., and S.C.V. helped on the experiments. S.C.V., M.L., and S.A.M. provided technical guidance and reviewed the manuscript.

Funding: This research was partially supported by DOE-NE Fuel Cycle Research and Development Program under the Contract number DE-AC52-06NA25396.

Acknowledgments: Authors would like to thank Carl Cady for his help with compression experiments, and Yukinori Yamamoto for providing FeCrAl materials. Also, the authors are grateful to Pete Baldo and Wei-Ying Chen for their help on conducting in situ annealing experiments at the Intermediate Voltage Electron Microscopy (IVEM)-Tandem Facility.

Conflicts of Interest: The authors declare no competing financial interests.

References

1. Klueh, R.L.; Harries, D.L. *High Chromium Ferritic and Martenitic Steels for Nuclear Applications*; ASTM: West Conshohocken, PA, USA, 2001.
2. Houdremont, E. *Handbook of Special Steels*, 3rd ed.; Springer: Berlin, Germany, 1956.
3. Odette, G.R.; Alinger, M.J.; Wirth, B.D. Recent Developments in Irradiation-Resistant Steels. *Annu. Rev. Mater. Res.* **2008**, *38*, 471–503. [[CrossRef](#)]
4. Hoelzer, D.T.; Bentley, J.; Sokolov, M.A.; Miller, M.K.; Odette, G.R.; Alinger, M.J. Influence of particle dispersions on the high-temperature strength of ferritic alloys. *J. Nuclear Mater.* **2007**, *367–370*, 166–172. [[CrossRef](#)]
5. Schneibel, J.H.; Liu, C.T.; Miller, M.K.; Mills, M.J.; Sarosi, P.; Heilmaier, M.; Sturm, D. Ultrafine-grained nanocluster-strengthened alloys with unusually high creep strength. *Scr. Mater.* **2009**, *61*, 793–796. [[CrossRef](#)]
6. Shen, J.; Yang, H.; Li, Y.; Kano, S.; Matsukawa, Y.; Satoh, Y.; Abe, H. Microstructural stability of an as-fabricated 12Cr-ODS steel under elevated-temperature annealing. *J. Alloys Compd.* **2017**, *695*, 1946–1955. [[CrossRef](#)]
7. Capdevila, C.; Chen, Y.L.; Jones, A.R.; Bhadeshia, H.K.D.H. Grain Boundary Mobility in Fe-Base Oxide Dispersion Strengthened PM2000 Alloy. *ISIJ Int.* **2003**, *43*, 777–783. [[CrossRef](#)]
8. Aydogan, E.; El-Atwani, O.; Takajo, S.; Vogel, S.C.; Maloy, S.A. High temperature microstructural stability and recrystallization mechanisms in 14YWT alloys. *Acta Mater.* **2018**, *148*, 467–481. [[CrossRef](#)]
9. Sallez, N.; Boulnat, X.; Borbély, A.; Béchade, J.L.; Fabrègue, D.; Perez, M.; de Carlan, Y.; Hennet, L.; Mocuta, C.; Thiaudière, D.; et al. In situ characterization of microstructural instabilities: Recovery, recrystallization and abnormal growth in nanoreinforced steel powder. *Acta Mater.* **2015**, *87*, 377–389. [[CrossRef](#)]
10. Naka, S.; Octor, H.; Bouchaud, E.; Khan, T. Reprecipitation observed in Y2O3 dispersed titanium during heat treatment after cold rolling. *Scr. Metall.* **1989**, *23*, 501–505. [[CrossRef](#)]
11. Sallez, N.; Hatzoglou, C.; Delabrouille, F.; Sornin, D.; Chaffron, L.; Blat-Yrieix, M.; Radiguet, B.; Pareige, P.; Donnadieu, P.; Bréchet, Y. Precipitates and boundaries interaction in ferritic ODS steels. *J. Nuclear Mater.* **2016**, *472*, 118–126. [[CrossRef](#)]
12. Gobernado, P.; Petrov, R.H.; Kestens, L.A.I. Recrystallized {311}⟨136⟩ orientation in ferrite steels. *Scr. Mater.* **2012**, *66*, 623–626. [[CrossRef](#)]
13. Kim, H.Y.; Kwon, O.Y.; Jang, J.; Hong, S.H. Modification of anisotropic mechanical properties in recrystallized oxide dispersion strengthened ferritic alloy. *Scr. Mater.* **2006**, *54*, 1703–1707. [[CrossRef](#)]
14. Aydogan, E.; Pal, S.; Anderoglu, O.; Maloy, S.A.; Vogel, S.C.; Odette, G.R.; Lewandowski, J.J.; Hoelzer, D.T.; Anderson, I.E.; Rieken, J.R. Effect of tube processing methods on the texture and grain boundary characteristics of 14YWT nanostructured ferritic alloys. *Mater. Sci. Eng. A* **2016**, *661*, 222–232. [[CrossRef](#)]
15. Ray, R.K.; Jonas, J.J. Transformation textures in steels. *Int. Mater. Rev.* **1990**, *35*, 1–36. [[CrossRef](#)]
16. Rios, P.R.; Siciliano, F., Jr.; Sandim, H.R.Z.; Plaut, R.L.; Padilha, A.F. Nucleation and growth during recrystallization. *Mater. Res.* **2005**, *8*, 225–238. [[CrossRef](#)]
17. Hoelscher, M.; Raabe, D.; Luecke, K. Rolling and recrystallization textures of bcc steels. *Steel Res.* **1991**, *62*, 567–575. [[CrossRef](#)]

18. Aydogan, E.; Maloy, S.A.; Anderoglu, O.; Sun, C.; Gigax, J.G.; Shao, L.; Garner, F.A.; Anderson, I.E.; Lewandowski, J.J. Effect of tube processing methods on microstructure, mechanical properties and irradiation response of 14YWT nanostructured ferritic alloys. *Acta Mater.* **2017**, *134*, 116–127. [[CrossRef](#)]
19. Wenk, H.R.; Lutterotti, L.; Vogel, S. Texture analysis with the new HIPPO TOF diffractometer. *Nuclear Instrum. Methods Phys. Res. A Accel. Spectrom. Detect. Assoc. Equip.* **2003**, *515*, 575–588. [[CrossRef](#)]
20. Aydogan, E.; Almirall, N.; Odette, G.R.; Maloy, S.A.; Anderoglu, O.; Shao, L.; Gigax, J.G.; Price, L.; Chen, D.; Chen, T.; et al. Stability of nanosized oxides in ferrite under extremely high dose self ion irradiations. *J. Nuclear Mater.* **2017**, *486*, 86–95. [[CrossRef](#)]
21. Aydogan, E.; Martinez-Saez, E.; March, K.; El-Atwani, O.; Krumwiede, D.L.; Hosemann, P.; Saleh, T.A.; Maloy, S.A. α' formation kinetics and radiation induced segregation/depletion in neutron irradiated 14YWT nanostructured ferritic alloys. *Sci. Rep.* under review.
22. Aydogan, E.; Weaver, J.S.; Carvajal-Nunez, U.; Schneider, M.M.; Gigax, J.G.; Krumwiede, D.L.; Hosemann, P.; Saleh, T.A.; Mara, N.A.; Hoelzer, D.T.; et al. Response of 14YWT alloys under neutron irradiation: A complementary study on microstructure and mechanical properties. *Acta Mater.* **2019**, *167*, 181–196. [[CrossRef](#)]
23. Lebensohn, R.A.; Tomé, C.N. A self-consistent anisotropic approach for the simulation of plastic deformation and texture development of polycrystals: Application to zirconium alloys. *Acta Metall. Mater.* **1993**, *41*, 2611–2624. [[CrossRef](#)]
24. Calcagnotto, M.; Ponge, D.; Demir, E.; Raabe, D. Orientation gradients and geometrically necessary dislocations in ultrafine grained dual-phase steels studied by 2D and 3D EBSD. *Mater. Sci. Eng. A* **2010**, *527*, 2738–2746. [[CrossRef](#)]
25. Burgers, W.G.; Masing, G. *Rekristallisation, Verformter Zustand und Erholung*; Akademische Verlagsgesellschaft Becker and Erler Kon: Leipzig, Germany, 1941.
26. Beck, P.A.; Hu, H. Recrystallization, grain growth and textures. In *The Origin of Recrystallization Textures*; American Society for Metals: Metals Park, OH, USA, 1966; pp. 393–433.
27. Humphreys, F.J.; Hatherly, M. *Recrystallization and Related Annealing Phenomena*; Elsevier Science: Jordan Hill, UK, 1995.
28. Johnson, W.A.; Mehl, R.F. Reaction kinetics in processes of nucleation and growth. *Trans. AIME* **1939**, *135*, 416–430.
29. Avrami, M. Kinetics of Phase Change. I General Theory. *J. Chem. Phys.* **1939**, *7*, 1103–1112. [[CrossRef](#)]
30. Kolmogorov, A.N. On the statistical theory of metal crystallization. *Izv. Akad. Nauk. SSSR Ser. Mater.* **1937**, *3*, 355–360.
31. Srolovitz, D.J.; Grest, G.S.; Anderson, M.P.; Rollett, A.D. Computer simulation of recrystallization—II. Heterogeneous nucleation and growth. *Acta Metall.* **1988**, *36*, 2115–2128. [[CrossRef](#)]
32. Malekjani, S.; Timokhina, I.B.; Wang, J.; Hodgson, P.D.; Stanford, N.E. Static recrystallization of strip cast alloys in the presence of complex nano-sulfide and nitride precipitates. *Mater. Sci. Eng. A* **2013**, *581*, 39–47. [[CrossRef](#)]
33. Xie, Z.-X.; Gao, H.-Y.; Wang, J.; Yu, Y.; Fang, Y.; Sun, B.-D. Static Recrystallization Behavior of Twin Roll Cast Low-Carbon Steel Strip. *J. Iron Steel Res. Int.* **2011**, *18*, 45–51. [[CrossRef](#)]
34. García-Mateo, C.; López, B.; Rodríguez-Ibabe, J.M. Static recrystallization kinetics in warm worked vanadium microalloyed steels. *Mater. Sci. Eng. A* **2001**, *303*, 216–225. [[CrossRef](#)]

